RSC Advances

ROYAL SOCIETY OF CHEMISTRY

PAPER

View Article Online
View Journal | View Issue

Check for updates

Cite this: *RSC Adv.*, 2025, **15**, 45840

Synthesis, optical features, and electrical properties of a new antimony-based hybrid halide $(C_8H_{14}N_2)[SbCl_5]$

Amin Alibi,[a] Nour Elleuch,[a] Abderrazek Oueslati,[b] Sergiu Shova[c] and Mohamed Boujelbene *[a]

Received 3rd September 2025
Accepted 12th November 2025

DOI: 10.1039/d5ra06615h

rsc.li/rsc-advances

A new antimony-based organic–inorganic hybrid, $(C_8H_{14}N_2)[SbCl_5]$, was synthesized by slow evaporation and characterized using complementary experimental and theoretical methods. Diffuse reflectance spectroscopy revealed a direct optical band gap of 2.77 eV, in close agreement with the DFT-predicted HOMO–LUMO gap of 2.7 eV. Under 259 nm excitation, the compound exhibits intense green–yellow photoluminescence at 571 nm, confirmed by CIE 1976 chromaticity coordinates. Differential scanning calorimetry shows three endothermic transitions (323, 358, 408 K) corresponding to structural reorganizations that modulate electrical behavior. Impedance spectroscopy evidences temperature-activated dielectric relaxation and strong interfacial polarization following a non-Debye mechanism. The modulus and conductivity analyses indicate multistep activation processes associated with phase transitions. DFT/TD-DFT calculations show charge transfer from $[SbCl_5]$ orbitals toward the pyridyl π-system, supported by MEP, ELF, LOL, and RDG-NCI analyses identifying key non-covalent interactions that stabilize the framework. Collectively, these results highlight $(C_8H_{14}N_2)[SbCl_5]$ as a structurally robust hybrid with tunable optical and dielectric responses suitable for photonic and thermally controlled optoelectronic applications.

1 Introduction

The pursuit of environmentally sustainable, lead-free materials for next-generation optoelectronic devices has directed increasing attention toward hybrid halide compounds, particularly those incorporating antimony(III) centers.[1,2] Owing to the stereoactive $5s^2$ lone pair of Sb^{3+}, these systems display pronounced local distortions that strongly influence their electronic configuration and give rise to remarkable photophysical and dielectric properties.[3,4] Among them, zero-dimensional (0D) antimony halides such as $(C_8H_{14}N_2)[SbCl_5]$ are especially notable for their broadband photoluminescence arising from self-trapped excitons generated through strong electron–phonon coupling within rigid polyhedral frameworks.[5,6] Their high photoluminescence quantum yields (PLQYs) make them attractive candidates for light-emitting and photonic applications.[7]

The optoelectronic performance of Sb(III)-based hybrids can be finely modulated through structural and compositional design. Adjusting halide anions or tuning the organic cation alters the band gap and emission profile, enabling precise control of absorption, color, and charge-transfer characteristics.[8,9] Several studies demonstrated that the incorporation of chiral or polar organic cations promotes non-centrosymmetric architectures with second-harmonic-generation (SHG) activity, enhancing nonlinear optical responses.[10,11] Similarly, controlled orientation of organic moieties yields anisotropic emission behavior suitable for polarized-light or tunable-emission devices.[12] Comparable structure–property relationships have been reported for other metal halides and perovskite-type hybrids, including orthorhombic chromites,[13] $LiNbO_3$-type oxides,[14] and bismuth halides,[15] reinforcing the importance of crystal symmetry and cation–anion interactions in tuning optical and dielectric responses.

Beyond optical tunability, Sb(III) hybrids exhibit rich electrical and dielectric behaviors characterized by large permittivity, frequency dispersion, and polarization relaxation phenomena. These features originate from the dynamic reorientation of dipolar cations and the polarizability of the inorganic sublattice.[16,17] Several Sb-based systems have even shown reversible spontaneous polarization, indicative of ferroelectric-like switching that is valuable for memory or sensor technologies.[18–20] Such multifunctional properties have spurred interest in integrating Sb(III) halide frameworks into

---

[a] *Laboratory of Physico-Chemistry of Solid State, LR11ES51, Sfax Faculty of Sciences, University of Sfax, Sfax 3000, Tunisia. E-mail: m_boujelbene2010@yahoo.fr*

[b] *Laboratory of Spectroscopic Characterization and Optical Materials, Department of Physics, Faculty of Sciences, University of Sfax, B.P. 1171, 3000 Sfax, Tunisia*

[c] *"Petru Poni" Institute of Macromolecular Chemistry, Alea Grigore Ghica voda 41-A, 700487 Iasi, Romania*

devices combining optical, electrical, and thermal functionalities.[21,22]

In this work, a new single-crystalline antimony-based hybrid, $(C_8H_{14}N_2)[SbCl_5]$, was synthesized by slow evaporation and investigated using complementary experimental and theoretical methods. Optical (UV-vis and photoluminescence), thermal (DSC), and dielectric analyses were combined with DFT and TD-DFT calculations to establish comprehensive structure–property correlations. The compound displays a direct optical band gap consistent with theoretical results, high PL efficiency, and multiregime dielectric relaxation behavior linked to its phase transitions. These characteristics, together with its lead-free composition and broad thermal stability,[23–27] highlight its potential for environmentally sustainable optoelectronic applications.

This study also forms part of a broader research framework aimed at understanding how a common organic cation $(C_8H_{14}N_2)$ influences the structure–property relationships across multiple Bi(III) and Sb(III) halometallate systems. The present work establishes the foundational electronic and dielectric characteristics of the Sb(III) compound, providing the reference point for comparative analysis in the subsequent study addressing functional and biological activities within the same hybrid family.[28]

2 Experimental

2.1 Materials and characterization techniques

The novel hybrid compound $(C_8H_{14}N_2)[SbCl_5]$ was synthesized from commercially available $SbCl_3$, HCl, and the organic precursor $C_8H_{12}N_2$ without further purification. The optical properties were measured by UV-vis diffuse reflectance spectroscopy (PerkinElmer Lambda 35, 200–1100 nm) and photoluminescence spectroscopy (PerkinElmer LS 55) at room temperature. Electrical impedance measurements were carried out using a Solartron SI 1260 impedance analyzer over 40 Hz–10^7 Hz and 40–140 °C (or 313–413 K) on pelletized samples (diameter = 6 mm, thickness = 1 mm). Additional instrumental details are provided in the SI.

2.2 Synthesis of $(C_8H_{14}N_2)[SbCl_5]$

The compound was obtained *via* a slow evaporation method by dissolving $C_8H_{12}N_2$ and $SbCl_3$ (1 : 1 molar ratio) in distilled water (10 mL), followed by the addition of concentrated HCl (38%). The solution was left undisturbed for four days, yielding colorless single crystals suitable for X-ray diffraction (Fig. 1). The material crystallizes in the monoclinic system, space group P21/*n*, consistent with our previously reported structure (CCDC 2382366).[29] After isolation, crystals were air-dried before further analysis.

Complementary details of the synthesis conditions and supporting structural validation (EDS, PXRD) are presented in the SI.

The compositional purity and structural integrity of the compound $(C_8H_{14}N_2)[SbCl_5]$ were initially evaluated using energy-dispersive X-ray spectroscopy (EDS) combined with elemental mapping, as presented in Fig. S1. The EDS spectrum, recorded at 20 kV and ×1000 magnification, exhibits exclusively the characteristic peaks of nitrogen, chlorine, and antimony, with no detectable contributions from other elements, confirming the high chemical purity of the synthesized material. The corresponding elemental maps reveal a homogeneous distribution of Cl and Sb across the crystalline domains, while the nitrogen signal indicates uniform incorporation of the organic cations within the hybrid lattice. Carbon and hydrogen are not observed in the EDS analysis, which is expected due to intrinsic limitations of the technique: hydrogen is undetectable owing to its extremely low atomic number, and carbon, although present in the organic cation, often produces weak or masked signals. Consequently, EDS predominantly provides reliable information on the heavier inorganic constituents, and the absence of any additional peaks beyond N, Cl, and Sb confirms the excellent compositional integrity of the material.

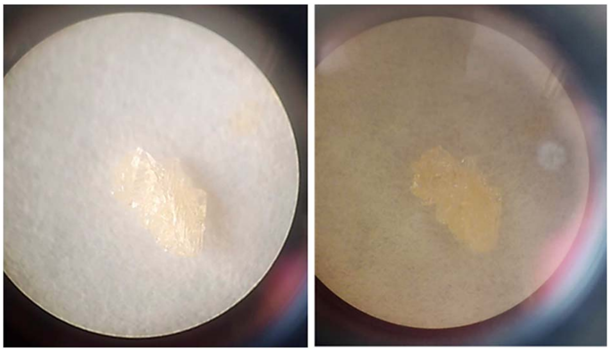

Fig. 1 Microscopic image of the $(C_8H_{14}N_2)[SbCl_5]$ compound.

Complementary structural characterization was performed *via* powder X-ray diffraction (PXRD), shown in Fig. S2. The experimental diffractogram (red curve) displays sharp, well-resolved reflections indicative of high crystallinity and closely matches the simulated pattern derived from single-crystal data (black curve). The precise agreement in both peak positions and intensities excludes the presence of secondary phases and validates the proposed structural model of the antimony–chloride hybrid. Together, the EDS and PXRD analyses unambiguously confirm the compositional and structural purity of $(C_8H_{14}N_2)[SbCl_5]$.

2.3 Thermal analysis

Differential scanning calorimetry (DSC) was performed on a 4.1 mg sample to investigate the compound's phase transitions. The DSC analysis was carried out using a PerkinElmer DSC 4000 calorimeter in an inert nitrogen atmosphere (N_2), with a heating and cooling rate of 5 °C min^{-1} over a temperature range from 25 °C to 180 °C (298–458 K).

2.4 Computational details

A detailed theoretical study was performed to examine the electronic and optical properties of the synthesized compound. UV-vis absorption, HOMO–LUMO energy gap, and advanced

DFT analyses were carried out using Multiwfn[30] with the hybrid B3LYP functional[31] and LanL2DZ basis set,[32] implemented in Gaussian 09 W.[33] A representative cluster containing one $(C_8H_{14}N_2)^{2+}$ cation and one $[SbCl_5]^{2-}$ anion was optimized to full convergence. Vibrational mode inspection *via* GaussView 6.0.16,[34] confirmed structural stability and the reliability of the theoretical predictions.

3 Results and discussion

3.1 Detailed optical study

3.1.1 Photoluminescence properties. Photoluminescence (PL) measurements were performed to examine the emission behavior and electronic transitions of $(C_8H_{14}N_2)[SbCl_5]$, providing key insight into its radiative processes. Under 259 nm excitation (Fig. 2(a)), the emission spectrum extends from 250 to 800 nm, covering much of the visible region. The spectrum features a strong, narrow band centered at 571 nm, characteristic of direct band-gap semiconductors where recombination occurs without momentum loss, indicating highly efficient radiative transitions. Additional weaker bands below 450 nm and between 550–650 nm suggest defect-assisted or localized excitonic emissions, reflecting minor lattice imperfections or interface effects within the hybrid lattice. The excitation spectrum (Fig. 2(b)) displays an intense peak at 414 nm, confirming the near-UV excitation as the most efficient for promoting the emissive state.

Complementary colorimetric analysis using the CIE 1976 chromaticity diagram (Fig. 3) yielded coordinates ($u' = 0.1789$, $v' = 0.5349$), corresponding to green–yellow emission. This emission lies in a region associated with high color purity and thermal stability, attributes favorable for optoelectronic and display applications. The green–yellow output also correlates with the material's direct band-gap value (2.77 eV), confirming consistent optical behavior between absorption and emission processes. Collectively, the PL and chromaticity analyses reveal a highly efficient emission mechanism and electronic structure well-suited for integration into light-emitting, sensing, and photonic devices.

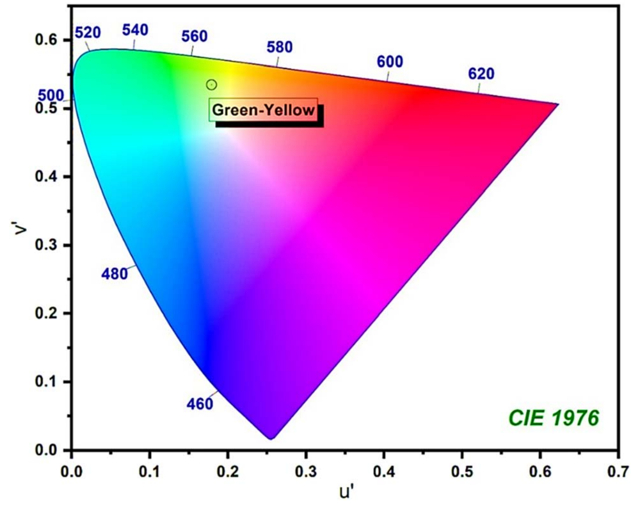

Fig. 3 Chromaticity diagram of $(C_8H_{14}N_2)[SbCl_5]$.

3.1.2 Diffuse reflectance spectroscopy (DRS). The diffuse reflectance (DR) spectrum, shown in Fig. 4, alongside its corresponding absorption spectrum, and the comparative analysis of DFT *vs.* the experimental absorption profile (Fig. S3), plays a pivotal role in assessing the optical response of $(C_8H_{14}N_2)[SbCl_5]$. Diffuse reflectance spectroscopy (DRS) is particularly suited for analyzing electronic transitions in powdered or polycrystalline samples, as it captures how incident light interacts with both surface and bulk regions. Applying the Kubelka–Munk (KM) transformation converts reflectance data into an absorption-like function, facilitating the determination of key optical parameters. In Fig. 4(a), the DR curve displays a sharp reflectance edge at 450 nm, indicating a distinct band gap transition. This steep drop reflects strong photon

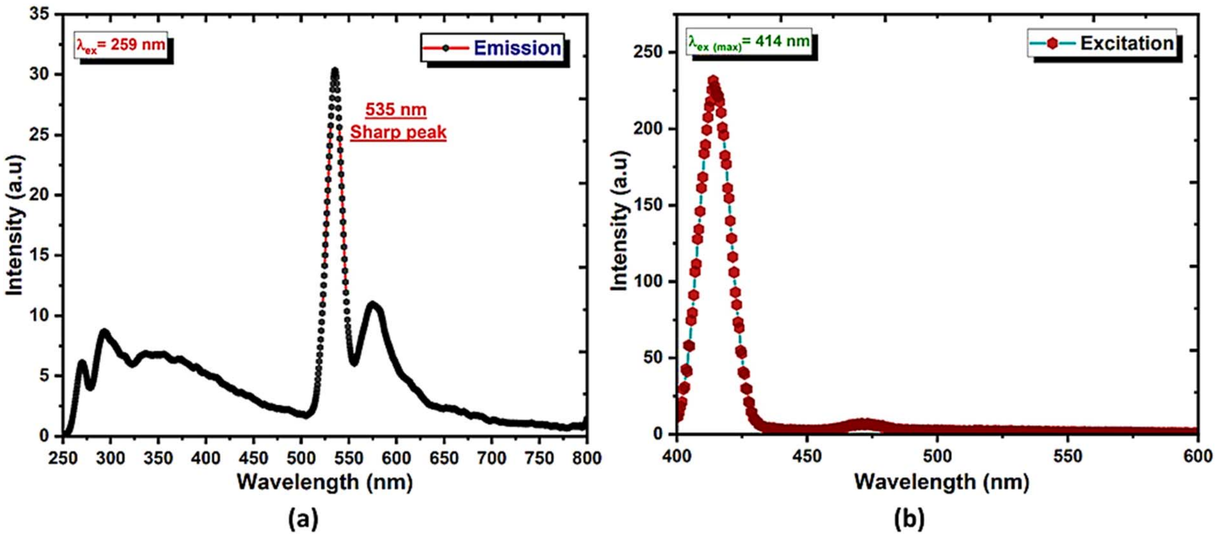

Fig. 2 (a) PL emission and (b) excitation plots of $(C_8H_{14}N_2)[SbCl_5]$.

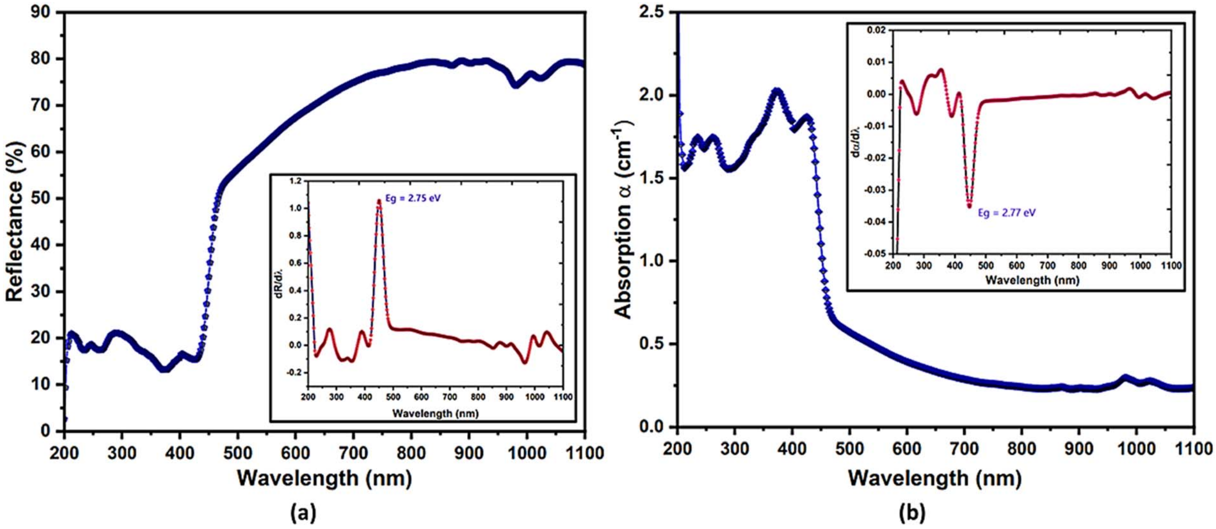

Fig. 4 (a) Diffuse reflectance, and (b) absorption spectrum, with their inset (derivatives).

absorption at the threshold and points to the direct band gap nature of the compound, where momentum-conserving transitions are efficient. The sharp edge also attests to good crystallinity and low structural disorder. The absorption spectrum (Fig. 4(b)) reveals four distinct peaks at 235, 262, 374, and 426 nm, each corresponding to unique electronic transitions in the hybrid system. DOS and PDOS analyses (Fig. 10) provide orbital-level interpretations and charge migration dynamics. The peaks at 235 and 262 nm are linked to hot electron–hole transitions within the $[SbCl_5]^{2-}$ anion, indicating excitation above the conduction band minimum followed by energy relaxation. These hot carriers affect optical absorption and carrier mobility. The 374 nm peak signifies a ligand-to-metal charge transfer (LMCT) from chloride (Cl 3p) to antimony (Sb 5p), reflecting strong electronic coupling in the anionic subunit. The 426 nm peak corresponds to the HOMO–LUMO transition, involving electron excitation from the $[SbCl_5]^{2-}$ orbitals (HOMO) to the π-system of the pyridine ring and nitrogen lone pair (LUMO), confirming charge transfer between inorganic and organic units, a key feature of hybrid materials. The calculated gap (2.7 eV) aligns closely with the experimental band gap (2.77 eV), validating this assignment. The KM function converts reflectance into an absorption coefficient-like curve (Fig. 4(b)), clearly revealing a strong absorption onset around 450 nm. This UV-visible range absorption highlights the material's capacity to capture high-energy photons effectively. Initial band gap estimation from derivative analysis (Fig. 5) yields a value of ∼2.75 eV, which will be refined using a Tauc plot (Fig. 5). Further corroboration through DOS, PDOS (Fig. 10), and Urbach energy analysis will offer additional insight into electronic transitions and possible tail states due to structural disorder. Overall, these optical results confirm the direct band gap behavior of $(C_8H_{14}N_2)[SbCl_5]$, forming a comprehensive basis for understanding its electronic and photonic performance.

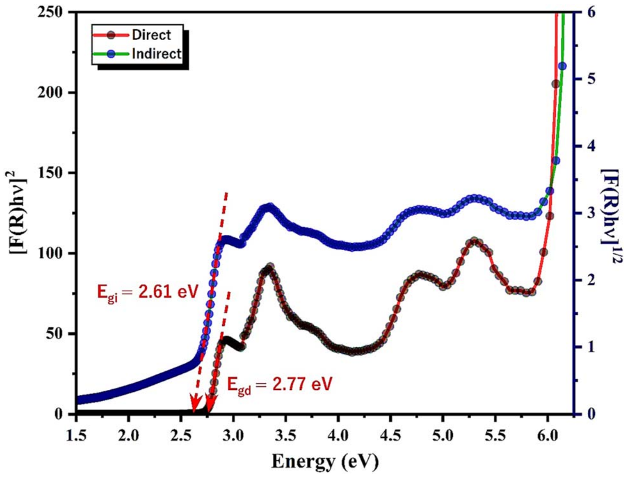

Fig. 5 Direct *vs.* indirect band gap determination *via* Tauc plot.

Fig. 5 presents the Tauc plot analysis used to determine the optical band gap of $(C_8H_{14}N_2)[SbCl_5]$. This method is essential for distinguishing between direct and indirect band gap transitions, a critical parameter influencing the material's optical and electronic properties. The Tauc plot using the Kubelka–Munk method was constructed by plotting $(F(R)h\nu)^n$ *vs.* photon energy ($h\nu$), where $F(R)$ is the absorption coefficient obtained from reflectance, h is Planck's constant, and ν is the photon frequency. The exponent n takes values of 2 for direct allowed transitions and 1/2 for indirect allowed transitions. The sharp reflectance edge observed at 450 nm in Fig. 4 already indicated a direct optical transition. This is further confirmed by the Tauc plot in Fig. 5, where the linear extrapolation of $(F(R)h\nu)^2$ *vs.* $h\nu$ yields an intercept at 2.77 eV, closely matching the reflectance-derived band gap value. The presence of a well-defined absorption edge without significant tailing suggests minimal structural disorder, reinforcing the direct band gap nature of the compound. The inset in Fig. 4 (derivatives of the reflectance and absorption spectra) already provided an approximate value for E_g, which aligns very closely, if not exactly, with the Tauc extrapolation in Fig. 5. This consistency across methods strengthens the reliability of the band gap determination, minimizing potential errors associated with baseline shifts or absorption tail effects. To further validate the experimentally derived band gap, density of states (DOS) analysis (Fig. 10) provides insights into the energy distribution of electronic states. The HOMO–LUMO gap obtained from theoretical calculations is 2.7 eV, which is in excellent agreement with the experimentally determined E_g of 2.77 eV. This close correlation between experimental and theoretical values confirms the electronic structure accuracy and highlights the strong interaction between the inorganic and organic moieties in defining the material's optical properties. This direct band gap nature suggests efficient radiative recombination processes, making the material suitable for applications in optoelectronic and photonic devices.

3.1.3 Determination of Urbach energy and threshold wavelength. Fig. 6 presents the Urbach energy (E_u) analysis, which provides insight into the degree of structural disorder and defect-induced localized states within $(C_8H_{14}N_2)[SbCl_5]$. The Urbach energy is extracted from the low-energy tail of the absorption spectrum, where the absorption coefficient (α) follows an exponential dependence on photon energy ($h\nu$), expressed in eqn (1) as:

$$(\alpha h\nu) = \alpha_0 \exp\left(\frac{h\nu}{E_u}\right) \tag{1}$$

where E_u is the Urbach energy, a key parameter indicating the extent of disorder and band tailing effects. A larger E_u suggests stronger structural distortions and increased electron–lattice interactions, while a lower E_u indicates a well-ordered crystalline system with minimal defect-related tail states.

In Fig. 6, the natural logarithm of the absorption coefficient, ln(α) is plotted against photon energy ($h\nu$). The linear region of this plot is fitted, and the inverse slope of the linear fit gives the Urbach energy E_u. The extracted value of $E_u = 177$ meV, which corresponds to 6.39% of the optical band gap ($E_g = 2.77$ eV). This relatively low percentage confirms that the material exhibits minimal structural disorder and retains a well-defined electronic band structure. The sharp absorption edge observed in Fig. 4 and 5 further supports this, reinforcing the conclusion that $(C_8H_{14}N_2)[SbCl_5]$ possesses a well-crystallized structure with a direct band gap.

The relatively small Urbach energy aligns with the sharp absorption onset (450 nm) in Fig. 4 and the well-defined band gap of 2.77 eV in Fig. 5, confirming that the material exhibits minimal band tailing effects. Additionally, Fig. 10 (DOS analysis) shows a clear energy separation between the valence and conduction bands, further validating that disorder-induced states do not significantly impact the band edges.

Fig. 6 confirms that $(C_8H_{14}N_2)[SbCl_5]$ has a low Urbach energy of 177 meV (6.39% of E_g), indicating minimal structural disorder and a well-defined band edge transition. The sharp absorption features and close agreement between experimental and theoretical band gaps confirm that defect-induced states play a negligible role, reinforcing the material's suitability for high-performance optoelectronic applications.

3.1.4 Penetration depth, optical extinction, and evolution of the refractive index. Fig. 7 illustrates the variation of the penetration depth (δ) as a function of wavelength (λ) for $(C_8H_{14}N_2)[SbCl_5]$. The penetration depth represents the distance at which incident photons can propagate into the material before their intensity decreases to $1/e$ (~37%) of the initial value due to absorption. It is a key optical parameter that influences light–matter interactions and determines the efficiency of photon absorption in semiconductors.

The penetration depth is inversely related to the absorption coefficient (α), following eqn (2):[35]

$$\delta = \frac{1}{\alpha} \tag{2}$$

where higher absorption coefficients correspond to shorter penetration depths (strong light absorption), and lower absorption coefficients result in longer penetration depths (weaker absorption).

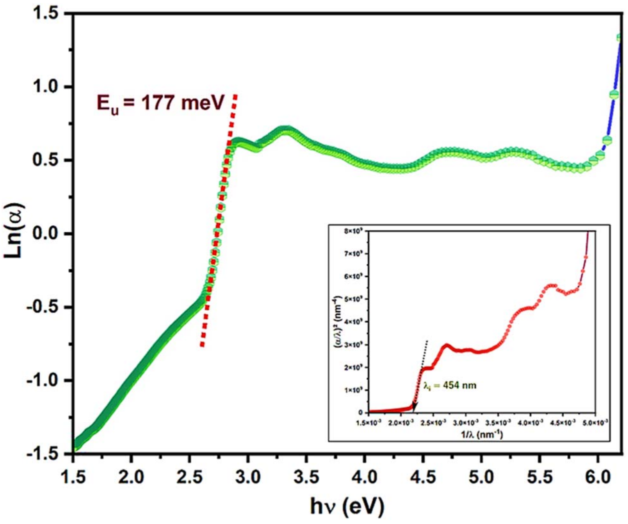

Fig. 6 Urbach energy analysis and the $(\alpha/\lambda)^2$ curve as a function of $1/\lambda$.

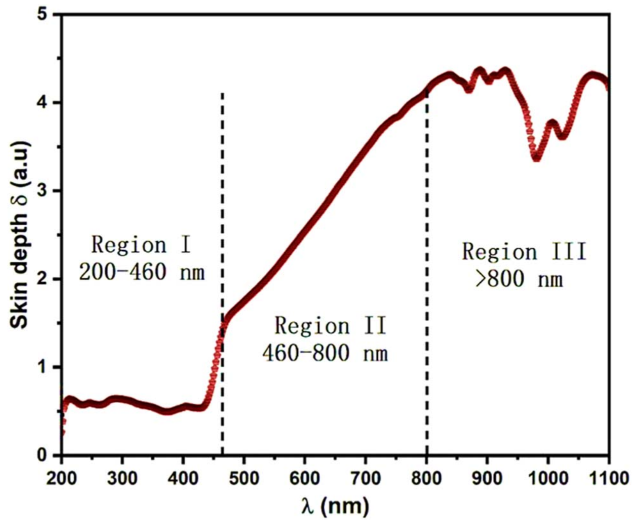

Fig. 7 Variation of penetration depth (δ) with wavelength (λ).

Fig. 7 reveals a strong wavelength dependence of the penetration depth:

- In the UV region (λ < 450 nm), where the material exhibits strong absorption (see Fig. 3 and 4), δ is relatively small, confirming that photons are efficiently absorbed within the near-surface region.
- As the wavelength increases beyond 450 nm, the penetration depth increases significantly, indicating reduced absorption in this spectral range. This trend is expected for semiconductors, where absorption is primarily strong near the band edge and diminishes at longer wavelengths.

At $\lambda \approx$ 450 nm, which corresponds to the optical absorption edge ($E_g \approx$ 2.77 eV, confirmed in Fig. 5), a transition in the penetration depth behavior is observed, marking the boundary between strong photon absorption and increased light penetration.

The penetration depth analysis is crucial for optimizing optoelectronic and photovoltaic applications. In materials with small δ in the visible range, efficient light harvesting occurs near the surface, making them suitable for thin-film-based devices. The observed penetration depth behavior of $(C_8H_{14}N_2)[SbCl_5]$ suggests that it can effectively absorb high-energy photons while allowing deeper light penetration at lower energies, a beneficial characteristic for light-emitting diodes (LEDs), photodetectors, and photovoltaic cells.

Fig. 8(a) presents the variation of the extinction coefficient (k) with wavelength (λ) for $(C_8H_{14}N_2)[SbCl_5]$. The extinction coefficient quantifies the material's ability to attenuate incident light due to absorption. A high k value indicates strong absorption, while a lower k suggests weak absorption or transparency at a given wavelength.

The extinction coefficient is directly related to the absorption coefficient (α) through eqn (3):[36]

$$k = \frac{\lambda\alpha}{4\pi} \tag{3}$$

where k follows the same trend as the absorption spectrum, peaking at wavelengths where electronic transitions occur.

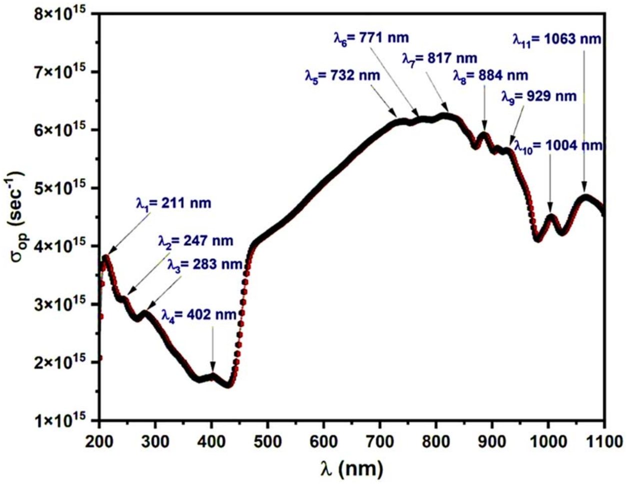

Fig. 9 Optical conductivity plot.

Fig. 8(a) shows that k exhibits a sharp increase in the UV region (λ < 450 nm), reaching its maximum near $\lambda \approx$ 426 nm, corresponding to the HOMO–LUMO transition (Fig. 4). This confirms strong absorption in the UV-visible region, consistent with the direct band gap nature of the material (E_g = 2.77 eV, Fig. 5).

Beyond 450 nm, the extinction coefficient decreases, indicating reduced absorption and increased light penetration in the longer-wavelength visible range, as corroborated by the penetration depth analysis (Fig. 7). The smooth decline in k suggests minimal defect-induced states, reinforcing the conclusion drawn from Urbach energy analysis (Fig. 6) that the material has low structural disorder.

The behavior of k is crucial in determining the material's optical conductivity, which will be further analyzed in Fig. 9. High k values in the UV region suggest strong interaction with photons, making $(C_8H_{14}N_2)[SbCl_5]$ a promising candidate for

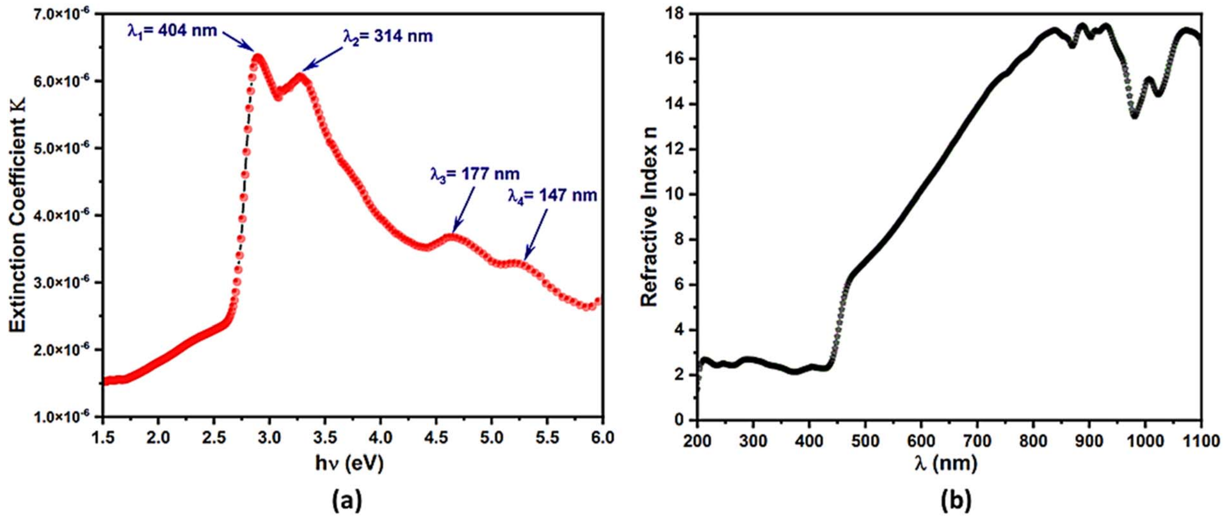

Fig. 8 (a) Variation of extinction coefficient (K) as a function of wavelength, (b) refractive index (n) plot.

UV photodetectors, solar cells, and optoelectronic devices that require efficient light absorption in this range.

Fig. 8(a) confirms that $(C_8H_{14}N_2)[SbCl_5]$ exhibits high extinction in the UV-visible range ($\lambda < 450$ nm), with a peak near 426 nm, corresponding to the HOMO–LUMO transition. The decreasing k at longer wavelengths suggests strong optical absorption near the band edge, making this material suitable for light-harvesting and optoelectronic applications. The low structural disorder inferred from the smooth k variation further supports its high optical quality.

Fig. 8(b) illustrates the variation of the refractive index (n) as a function of photon energy for the hybrid organic–inorganic compound $(C_8H_{14}N_2)[SbCl_5]$, providing key insights into its dielectric response and light–matter interaction behavior. The optical refractive index n change can be explained by the following eqn (4):[37]

$$n(\lambda) = \frac{1 + R + \sqrt{4R - (1 - R)^2 K^2}}{1 - R} \tag{4}$$

The refractive index is observed to exhibit a sharp rise as the photon energy approaches the absorption edge, followed by a gradual decline at higher energies, consistent with the normal dispersion regime characteristic of semiconducting materials. The initial peak near the band edge confirms the strong polarizability of the lattice at energies just below the electronic transitions, highlighting the high optical density in this region.

The sharp rise as photon energy approaches the absorption edge behavior correlates well with the direct band gap previously extracted from the Tauc plot and the absorption spectrum, suggesting the refractive index enhancement stems from decreased electronic transition probabilities near the optical onset. The observed peak position of the refractive index also provides indirect validation of the band structure and indicates a relatively low energy-loss regime, supporting the material's potential for photonic and optoelectronic applications. Furthermore, the smooth decline in n with increasing photon energy reflects the reduced interaction between incident photons and bound electrons at higher energies, confirming the stability of the optical properties in the ultraviolet regime.

3.1.5 Optical conductivity analysis. Fig. 9 illustrates the optical conductivity (σ) variation as a function of wavelength (λ) for $(C_8H_{14}N_2)[SbCl_5]$. Optical conductivity is a crucial parameter that quantifies the material's response to incident electromagnetic radiation, describing how efficiently it can absorb and transport photogenerated charge carriers. It is directly related to the dielectric function and extinction coefficient, making it an essential factor in evaluating a material's suitability for optoelectronic applications.

The optical conductivity $\sigma(\omega)$ is derived from the extinction coefficient (k) and the refractive index (n) using eqn (5):

$$\sigma_{\text{op}} = \frac{\alpha(\lambda)n(\lambda)c}{4\pi k_e(\lambda)} \tag{5}$$

where c, α, k_e, and n represent the speed of light in free space (or air), the absorption coefficient, the extinction coefficient, and the refractive index, respectively.

Fig. 9 shows a sharp increase in optical conductivity starting from 450 nm, with a prominent peak around 426 nm, which confirms that photon absorption in this region leads to a significant increase in charge carrier excitation, reinforcing the direct band gap nature of the material ($E_g = 2.77$ eV, Fig. 5). Beyond 450 nm, optical conductivity increases significantly, reaching a maximum around 800 nm, followed by fluctuations at longer wavelengths. This indicates enhanced light absorption and effective photogenerated charge carrier generation in the visible to near-infrared region. The increasing optical conductivity suggests the presence of secondary electronic transitions or defect-related states, highlighting complex light–matter interactions. The peaks observed in the UV-visible range confirm highly efficient photo-induced electron transitions, supporting potential applications in light-harvesting and optoelectronic devices. The strong correlation between optical conductivity and the refractive index (Fig. 8(b)) suggests high optical interaction, making $(C_8H_{14}N_2)[SbCl_5]$ a promising candidate for photodetectors and optical modulators.

Optical conductivity is directly related to the imaginary part of the dielectric function, which will be further analyzed in Fig. 10 to provide a deeper understanding of charge polarization

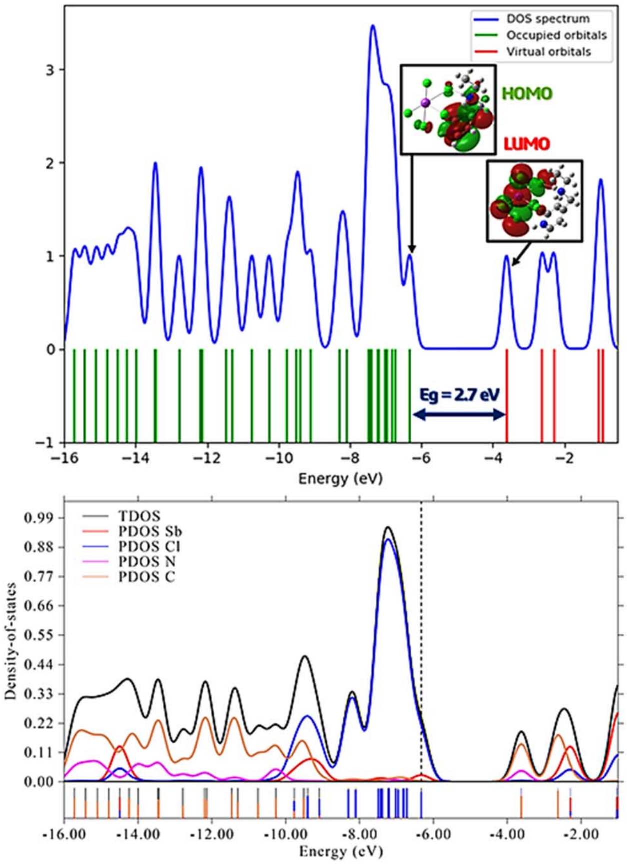

Fig. 10 Total and partial density of state ((DOS) and (PDOS)) spectra, and the FMO.

effects. The observed trend suggests high efficiency in photo-induced charge carrier generation, reinforcing its suitability for photodetectors, photovoltaic devices, and other optoelectronic applications requiring efficient light–matter interaction.

3.2 Theoretical investigation

3.2.1 Frontier molecular orbital (FMO) analysis. The Frontier molecular orbitals are crucial in determining a compound's electrical and optical properties, as well as its chemical reactions. The HOMO (Highest Occupied Molecular Orbital) represents a molecule's ability to donate electrons, while the LUMO (Lowest Unoccupied Molecular Orbital) represents its ability to accept electrons. The HOMO–LUMO gap is an essential factor in determining the hardness or softness of a molecule. A larger gap indicates a "hard" molecule, whereas a smaller gap indicates a "soft" molecule, which implies higher reactivity. The chemical reactivity of a compound is directly proportional to its hardness, with a lower HOMO–LUMO gap indicating greater activity. By analyzing the frontier molecular orbitals at different energy levels, we can determine the band gap values of the compound mentioned in the title. The DOS (density of states) spectrum was generated using Gauss-Sum 3.0 software,[38] and the distribution of the HOMO and LUMO orbitals can be seen in Fig. 10.

Koopman's theorem[39,40] can be applied to calculate the ionization potential (μ) of the compound. According to this theorem, μ is half the sum of $E_{(\mathrm{HOMO})}$ and $E_{(\mathrm{LUMO})}$. The EI can be determined using the negative value of $E_{(\mathrm{HOMO}),}$ and the E_{A} can be obtained using the negative value of $E_{(\mathrm{LUMO})}$. The global chemical hardness (η), softness (S), electrophilicity (ω) indices, and electronegativity (χ) can also be expressed, respectively, by $\eta = 1/2(E_{(\mathrm{LUMO})} - E_{(\mathrm{HOMO})})$, $S = E_{\mathrm{I}}/2\eta$, $\omega = \mu^2/2\eta$, and $\chi = 1/2(E_{\mathrm{I}} + E_{\mathrm{A}})$. The corresponding values for orbital energy, energy gap, hardness, and softness can be found in Table S1. The energy calculations and graphical output were performed using the DFT/B3LYP/LanL2DZ basis set. Additionally, the electronic absorption properties of the compound were analyzed by performing a calculation using time-dependent density functional theory (TD-DFT) in water solvent.

The UV-vis spectrum for three excited states of the compound is displayed in Fig. S4. Table S2 provides the calculated electronic absorption wavelengths, oscillator strengths, and major contributions to the electronic transitions. The absorption peak at 365 nm, which is the strongest one, is due to a transition between HOMO and LUMO, with a 97% contribution by the charge flow from the electron orbitals of chloride and antimony atoms of the $\mathrm{SbCl_5}$ anionic entity to the π-electron orbitals of the pyridine and the lone pair orbital of the N atom belonging to the ramification, as shown in Fig. S5. This means a charge migration from the inorganic to the organic part. The HOMO–LUMO gap, which is the energy difference between the HOMO and LUMO, has been calculated to be 2.7 eV, and it is very consistent with the experimental value of 2.77 eV. The absorption peak at 357 nm is caused by H−1 to LUMO and H−1 to L+1 transitions. These absorptions were attributed to the charge flow from the orbitals of the base four chloride atoms belonging to the antimony pentachloride complex to the π-electron orbitals of the pyridine and lone pair orbital of the N atom belonging to the ramification, and to the π-electron orbitals of the pyridine and the orbital of antimony. This transition has the lowest oscillator strength, with a 95% and 3% contribution to the total contributions of the transition, respectively. The last absorption at 342 nm is a HOMO to L+1 transition, with a 98% contribution to the total contributions of the transition. It was considered as a charge flow between the electrons of HOMO orbitals, located at the anionic entity to the antimony atom, and the orbitals of the π-electron orbitals of the pyridine.

3.2.2 MEP, NCI-RDG, ELF, and LOL analyses. The electronic structure properties and intermolecular interactions of the hybrid compound $(\mathrm{C_8H_{14}N_2})[\mathrm{SbCl_5}]$ are thoroughly examined using Molecular Electrostatic Potential (MEP), Non-Covalent Interaction Reduced Density Gradient (NCI-RDG), Electron Localization Function (ELF), and Localized Orbital Locator (LOL) analyses. These computational tools provide a detailed understanding of charge distribution, weak interactions, electron localization, and bonding nature, offering critical insights into the compound's stability, reactivity, and potential applications.

The MEP analysis maps the electrostatic potential across the molecular surface, identifying electrophilic and nucleophilic regions. This information is crucial for predicting reactive sites and understanding intermolecular interactions such as hydrogen bonding and electrostatic stabilization. NCI-RDG analysis complements this by visualizing weak forces like van der Waals interactions and hydrogen bonds, shedding light on the supramolecular architecture and packing efficiency. The ELF and LOL analyses further refine the electronic picture by characterizing the localization of electron density and orbital interactions. The ELF function highlights regions of strong electron pairing, such as covalent bonds and lone pairs, while the LOL analysis identifies orbital localization patterns, distinguishing between bonding and non-bonding interactions. Together, these methods provide a holistic view of the electronic distribution and bonding framework of $(\mathrm{C_8H_{14}N_2})[\mathrm{SbCl_5}]$, allowing for a deeper interpretation of its structural stability and functional properties. By integrating these advanced computational analyses, a deeper, comprehensive electronic and structural profile of the compound emerges, bridging theoretical predictions with experimental insights, and facilitating its characterization and potential applications in materials science and optoelectronics.

3.2.3 Molecular electrostatic potential MEP analysis. The Molecular Electrostatic Potential (MEP) analysis of $(\mathrm{C_8H_{14}N_2})[\mathrm{SbCl_5}]$ provides a detailed representation of the charge distribution across the molecular surface, offering crucial insights into its electronic properties and potential interaction sites. The MEP map in Fig. S6, reveals regions of high electron density, shown in red, which correspond to nucleophilic sites, while blue regions indicate electron-deficient areas prone to electrophilic interactions.

In this compound, the most negatively charged regions are localized around the chlorine atoms in the $[\mathrm{SbCl_5}]^{2-}$ unit, reflecting their strong electron-withdrawing nature and their role as hydrogen bond acceptors. Conversely, the highest positive electrostatic potential is concentrated around the hydrogen atoms of the $(C_8H_{14}N_2)^{2+}$ organic cation, particularly near the protonated nitrogen centers, signifying their function as hydrogen bond donors. This charge distribution strongly influences the compound's ability to form a stable hydrogen-bonding network, contributing to its structural integrity.

The asymmetry in the electrostatic potential suggests directional interactions between the organic and inorganic components, reinforcing the hybrid nature of the compound. Additionally, the balanced charge distribution between the organic cation and the $[SbCl_5]^{2-}$ anion promotes electrostatic stabilization, which plays a critical role in crystal packing and lattice energy optimization. These findings underscore the significance of MEP analysis in predicting the compound's reactivity and interaction pathways, aiding in the rational design of materials with tailored electronic and supramolecular properties.

3.2.4 Non-covalent interaction NCI-RDG analysis. The Non-Covalent Interaction Reduced Density Gradient (NCI-RDG) analysis of $(C_8H_{14}N_2)[SbCl_5]$ provides an in-depth visualization of weak intermolecular forces that stabilize the crystal structure (Fig. S7). This method distinguishes attractive, repulsive, and neutral interactions using a color-coded mapping system, where blue regions indicate strong hydrogen bonding, green regions represent van der Waals forces, and red regions highlight steric repulsions.

In this compound, the $[SbCl_5]^{2-}$ anion forms significant non-covalent interactions with the $(C_8H_{14}N_2)^{2+}$ cation through hydrogen bonding, particularly between the protonated nitrogen atoms of the organic moiety and the chlorine atoms of the anion. These stabilizing interactions, shown as blue regions in the NCI isosurface, contribute to the structural cohesion of the hybrid framework. The presence of green regions around the organic cation indicates weak dispersion forces that further influence crystal packing.

Additionally, minimal steric repulsion (red regions) suggests an optimized molecular arrangement with limited destabilizing interactions, reinforcing the efficiency of the packing structure. The balance between hydrogen bonding and van der Waals forces observed in the NCI-RDG analysis plays a key role in determining the stability and supramolecular organization of $(C_8H_{14}N_2)[SbCl_5]$. These findings provide valuable insights into the compound's potential for applications where non-covalent interactions are critical, such as in crystal engineering and functional material development.

3.2.5 Electron localization function (ELF) and localized orbital locator (LOL) analyses. Fig. S8 presents the crystallographic projections of $(C_8H_{14}N_2)[SbCl_5]$ along the (XY), (XZ), and (YZ) planes, offering a precise geometrical framework for interpreting the spatial organization and bonding environment of the compound. This structural reference is essential for correlating electronic behavior with atomic arrangements, revealing the orientation of the $[SbCl_5]^{2-}$ anions relative to the $(C_8H_{14}N_2)^{2+}$ cations and highlighting potential sites of electrostatic interaction, hydrogen bonding, and van der Waals contacts. Based on this framework, the Electron Localization Function (ELF) map in Fig. S9(a) provides detailed insight into the electron density topology, indicating strongly localized regions around the chlorine atoms of the $[SbCl_5]^{2-}$ moiety, corresponding to nonbonding lone pairs, which serve as key hydrogen bond acceptors. The Sb center displays moderate localization, reflecting a partially delocalized coordination environment typical of hypervalent p-block centers. Within the organic cation, highly localized electron density is observed near the nitrogen atoms, confirming their active role in hydrogen bonding through lone pair donation. These ELF findings emphasize the directional and structured nature of the non-covalent interaction network, reinforcing the compound's supramolecular integrity and supporting the existence of significant charge delocalization between the organic and inorganic fragments. Complementary insights are provided by the Localized Orbital Locator (LOL) map in Fig. S9(b), which reveals spatial distributions of orbital localization across the compound. The LOL profile identifies sharply localized orbitals near the Cl atoms and moderate delocalization at the Sb center, while confirming substantial orbital localization around the nitrogen atoms in the cation. These observations, when referenced against the three-plane projections in Fig. S8, validate the spatial alignment of donor–acceptor interactions and van der Waals forces within the lattice. The synergy between the ELF and LOL analyses demonstrates the complementary nature of localized and delocalized bonding characteristics in stabilizing the hybrid framework. Together, these results not only clarify the charge distribution, bonding pathways, and electron pairing behavior across the system but also underscore the importance of weak intermolecular forces in directing the structural cohesion and potential electronic transport pathways. This integrated topological perspective reinforces the compound's potential for targeted applications in solid-state functional materials and hybrid optoelectronic platforms.

3.3 Thermal analysis: differential scanning calorimetry analysis

Fig. 11 presents the Differential Scanning Calorimetry (DSC) curve of the $(C_8H_{14}N_2)[SbCl_5]$ hybrid compound, revealing three distinct endothermic transitions at 320 K, 366 K, and 403 K. These thermal events signify phase transitions, which are corroborated by the conductivity shifts observed in the Arrhenius plot (Fig. 14), confirming their direct impact on the electrical behavior. The correspondence between these thermal anomalies and the abrupt changes in impedance characteristics highlights the strong coupling between structural dynamics and ionic transport, a feature commonly investigated using Electrochemical Impedance Spectroscopy (EIS). This interrelation emphasizes the compound's thermally tunable conductivity, essential for designing temperature-responsive electronic materials.

3.4 Electrical properties (electrical impedance spectroscopy)

3.4.1 Complex impedance analysis (Nyquist plots). The complex impedance (Nyquist) plots of $(C_8H_{14}N_2)[SbCl_5]$

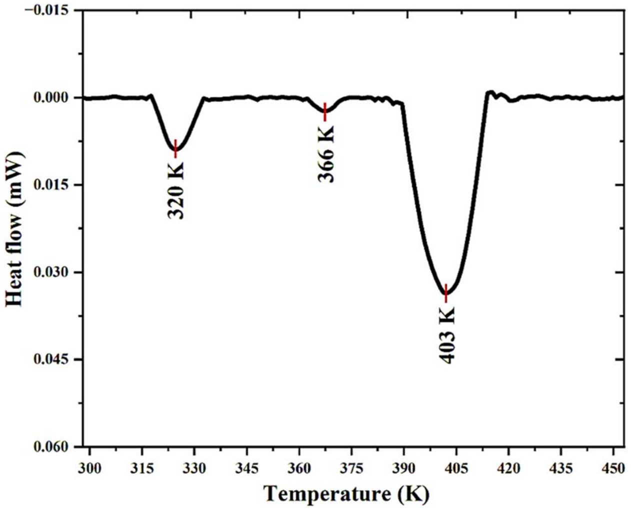

Fig. 11 Thermal behavior analysis of $(C_8H_{14}N_2)[SbCl_5]$ using differential scanning calorimetry.

recorded between 313 and 413 K (Fig. 12) display single, well-defined semicircular arcs across all temperatures, confirming a dominant bulk-controlled relaxation process. The spectra were modeled using an equivalent circuit consisting of Rs–L_1 in series with two parallel CPE–R branches, effectively reproducing the non-ideal, distributed relaxation behavior characteristic of non-Debye systems. The inclusion of L_1 accounts for minor inductive effects arising from sample geometry and measurement leads at high frequencies. The semicircle diameters decrease with rising temperature, consistent with thermally activated charge transport and reduced overall resistance. Notably, discontinuous changes in semicircle size at specific temperature intervals indicate phase-dependent conduction regimes correlated with the DSC transitions. The largest arc appears at 313 K, followed by a moderate reduction between 323–353 K, further contraction at 363–403 K, and the smallest at 413 K, demonstrating structural and electronic reorganization with heating. These variations likely originate from temperature-induced rearrangements of Sb–Cl bonds and re-orientation of the organic cation, which alter carrier mobility and interfacial polarization dynamics.

The frequency-dependent real and imaginary impedance components, $Z'(f)$ and $Z''(f)$ (Fig. 13), provide complementary insights into the relaxation behavior. $Z'(f)$ decreases sharply with frequency in low regions, reflecting space-charge

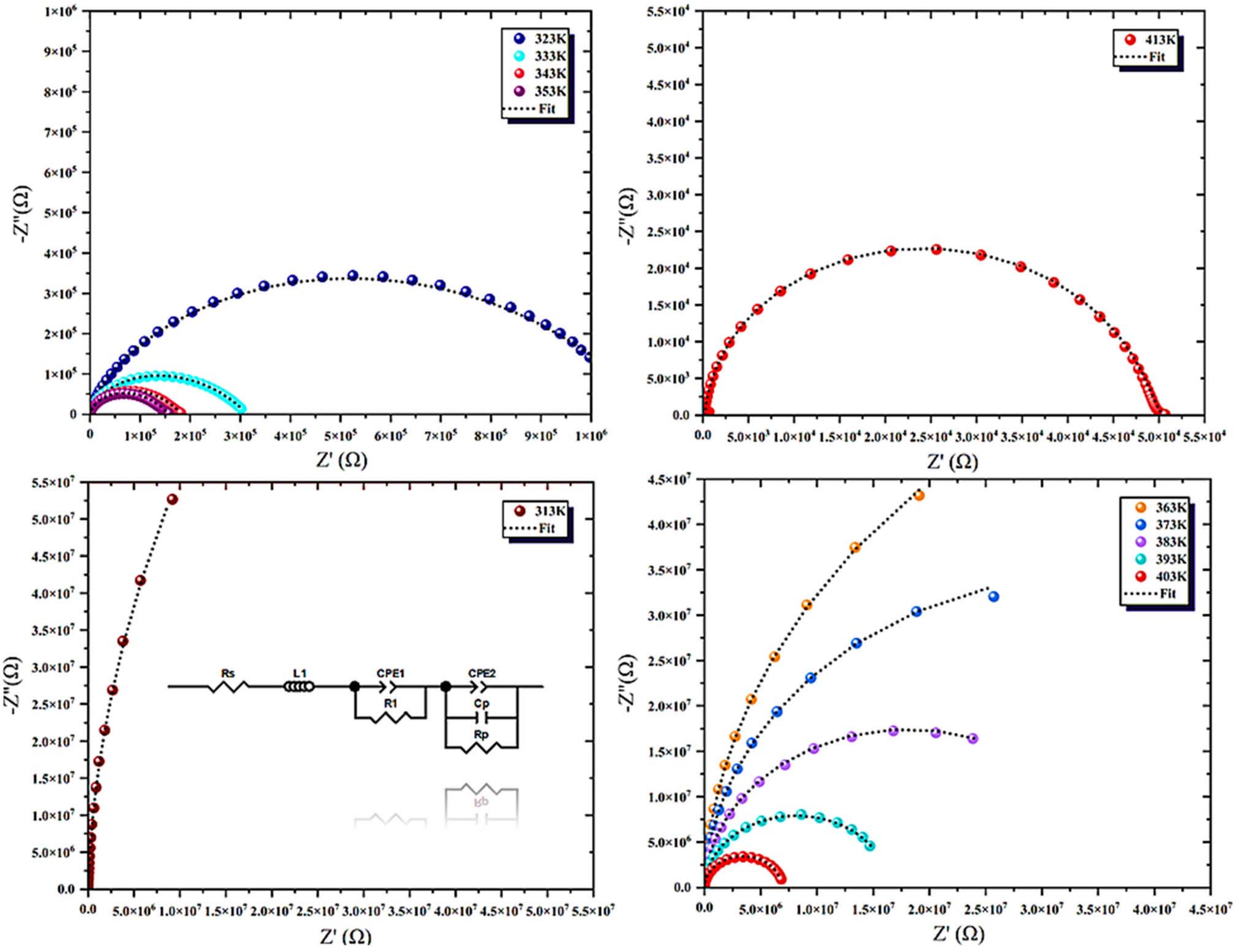

Fig. 12 Nyquist plots at different temperatures ($-Z''$ vs. Z').

polarization and interfacial effects, and becomes nearly frequency-independent at high frequencies, indicating the onset of bulk conduction. $Z''(f)$ exhibits distinct relaxation peaks whose maxima shift toward higher frequencies with increasing temperature, signifying thermally activated relaxation governed by the relation $\omega_{\max} = 1/\tau$. Four distinct temperature domains: 313 K, 323–353 K, 363–403 K, and 413 K, which are clearly identified, each showing a specific relaxation profile associated with the structural phases. The lower-temperature regime shows high-amplitude, low-frequency peaks indicating slow polarization, while the highest-temperature regime exhibits narrow, high-frequency peaks corresponding to enhanced ionic mobility and reduced potential barriers. These transitions confirm that polarization and conduction mechanisms are strongly phase-dependent and intimately linked to the hybrid's thermally induced structural evolution.

Comparison between experimental and simulated spectra (Fig. S10) using nonlinear least-squares fitting demonstrates excellent agreement across all frequencies, validating the robustness of the selected equivalent circuit (Fig. 12). The high-quality fits confirm that the complex electrical behavior of $(C_8H_{14}N_2)[SbCl_5]$ arises from a combination of bulk and interfacial contributions, with non-ideal capacitive and distributed relaxation effects accurately captured by the model. Overall, the impedance analysis reveals a dynamic electrical response controlled by multiple temperature-dependent conduction regimes, tightly coupled to the material's intrinsic structural reorganization.

3.4.2 Conductivity analysis. Fig. 14 displays the Arrhenius behavior of the compound, where the thermal evolution of the electrical conductivity is expressed in the form of $\ln(\sigma \times T)$ *versus* $1000/T$. The graph reveals four distinct temperature regimes, consistent with the phase transitions inferred from the impedance analysis. However, due to limited data points at the extremities (313 K and 413 K), only the two central domains, covering the ranges from 323 K to 353 K and from 363 K to 403 K, are suitable for reliable kinetic analysis. Linear fitting of these two domains yields two clear activation energies: $E_{a_1} = 0.39$ eV for the lower-temperature phase and $E_{a_2} = 0.97$ eV for the higher-temperature phase. This sharp increase in activation energy between the two phases implies a substantial alteration in the charge carrier dynamics and transport barriers, likely arising from structural rearrangements or changes in the interaction between the antimony-iodine octahedra and the organic moieties.

The lower activation energy ($E_{a_1} = 0.39$ eV) suggests relatively facile ionic or polaronic transport in the low-temperature phase, a value consistent with those reported for various hybrid halide perovskites and low-dimensional organometallic materials. For example, similar values have been reported for La-doped perovskite ceramics where E_a ranged between 0.3–0.4 eV, linked to moderate ion migration across perovskite cages.[41] On the other hand, the higher activation energy ($E_{a_2} = 0.97$ eV) is comparable to that observed in certain defect-rich oxide materials or highly resistive hybrid systems, such as strontium lanthanum gallates or certain tungsten-doped thioantimonate solid-state electrolytes.[42,43] This substantial energy barrier is indicative of either deeper trap states, increased lattice rigidity, or suppressed ionic mobility in the higher-temperature phase of the material. Such an abrupt transition in transport energetics underscores the critical role of phase transitions in modulating the conductive pathways within hybrid frameworks. The coexistence of low- and high-barrier conduction domains offers a unique platform for temperature-tuned functionality, especially in applications where selective phase-dependent transport is desirable, such as in smart resistive switches or tunable energy-storage devices.

3.4.3 Complex modulus analysis (electrical conduction mechanisms). Fig. 15 presents the complex electric modulus spectra of $(C_8H_{14}N_2)[SbCl_5]$, depicting the real (M') and imaginary (M'') components as functions of frequency at various temperatures. The modulus formalism, defined as $M = 1/\varepsilon^* =$

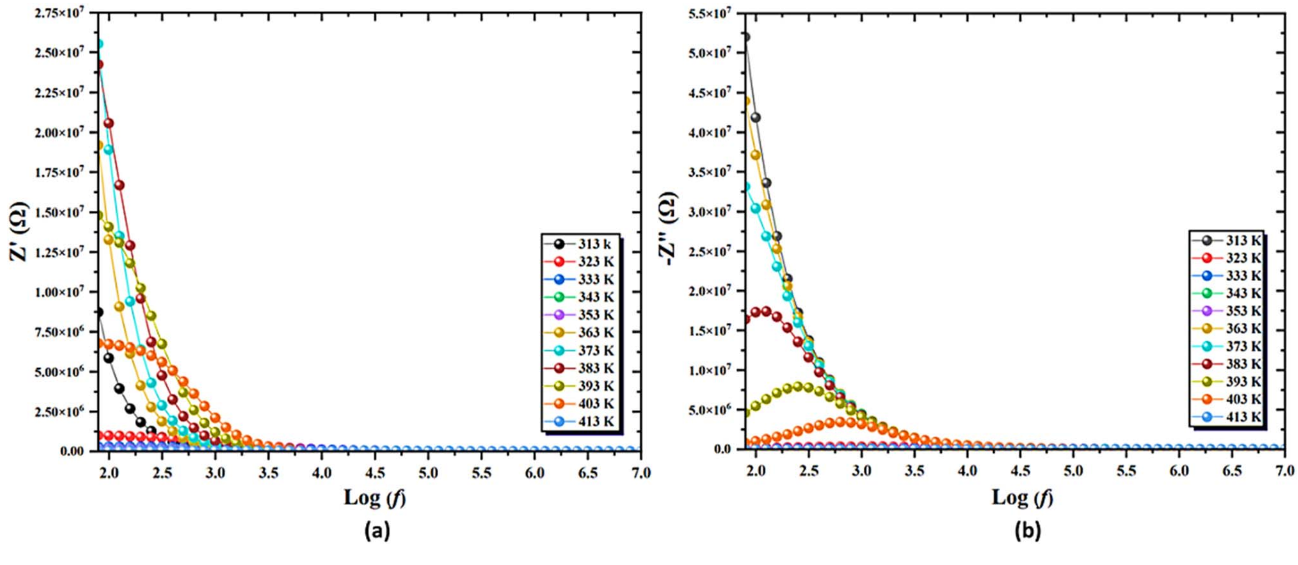

Fig. 13 Frequency dependence of impedance components Z' (a) and Z'' (b) $= f(\log(f))$.

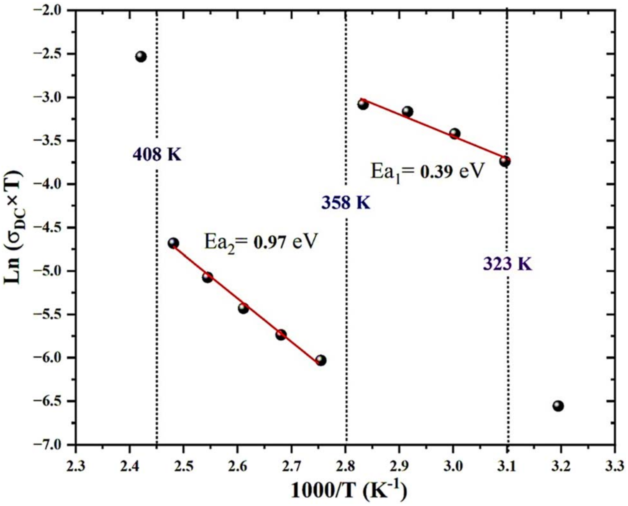

Fig. 14 Thermal Activation of Conductivity $\ln(\sigma \times T) = f(1000/T)$.

$M' + jM''$, minimizes electrode polarization effects and isolates intrinsic relaxation phenomena, particularly relevant for non-Debye systems like this hybrid compound. In the M' spectra, values remain close to zero at low frequencies, confirming negligible long-range conduction, then increase with frequency and saturate at high values, reflecting the transition from interfacial polarization to bulk relaxation. The modest upward shift of M' with temperature indicates thermally activated charge motion and enhanced dielectric rigidity.

The M'' spectra exhibit single, well-resolved peaks that shift toward higher frequencies as temperature rises, demonstrating thermally activated relaxation and decreasing relaxation time (τ). The peak asymmetry and broadening at intermediate temperatures confirm a distribution of relaxation times, consistent with the constant phase element (CPE) behavior derived from impedance modeling. The clear separation between temperature-dependent M'' peaks delineates two primary activation domains: a low-temperature region ($E_{a_1} = 0.39$ eV) characterized by broad, low-frequency peaks associated with restricted dipolar reorientation, and a high-temperature region ($E_{a_2} = 0.97$ eV) with sharper, high-frequency peaks indicative of increased carrier mobility and reduced lattice coupling.

This progressive shift and narrowing of M'' peaks correlate strongly with the Arrhenius conductivity behavior, confirming that both conduction and relaxation processes are governed by the same temperature-induced structural transitions. The modulus representation thus highlights localized, short-range carrier motion that remains masked in impedance spectra. Such temperature-sensitive dielectric relaxation underscores the compound's potential for ion-conducting, energy-storage, and tunable dielectric applications, where localized polarization dynamics play a decisive functional role.

3.5 Dielectric constant

Fig. 16 presents the dielectric response of the synthesized hybrid compound, illustrating both the real (ε') and imaginary (ε'') parts of the permittivity as functions of frequency and temperature. The full-range spectra in the left panels show a strong dispersion in both ε' and ε'' at low frequencies, which systematically diminishes with increasing frequency, eventually converging toward frequency-independent plateaus. This characteristic behavior reflects the intrinsic dielectric relaxation of the material, where space charge and interfacial polarization dominate at low frequencies, while high-frequency responses capture more intrinsic lattice-related dielectric properties. The dramatic decrease in ε' across several orders of magnitude, from values as high as $\sim 10^4$ at low frequencies down to ~ 10–10^2 at higher frequencies, is a clear signature of Maxwell–Wagner-type interfacial polarization, often observed in polycrystalline or hybrid systems where layered or phase-separated regions coexist. The corresponding ε'' profiles exhibit similar trends,

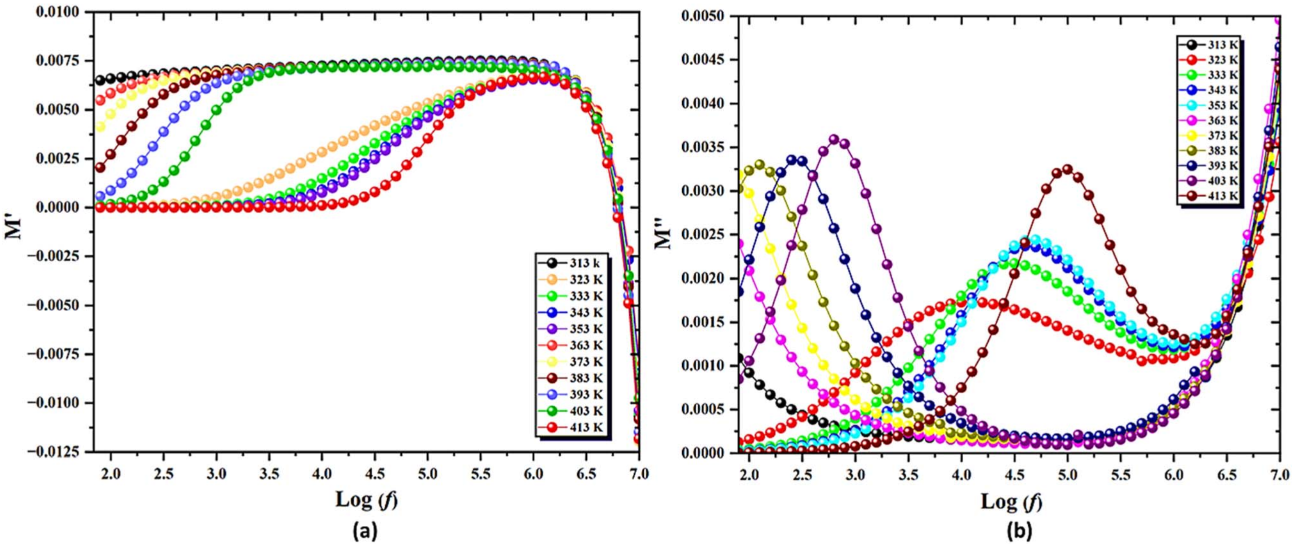

Fig. 15 Frequency dependence of (a) the real (M') and (b) imaginary (M'') parts of the complex electric modulus at different temperatures.

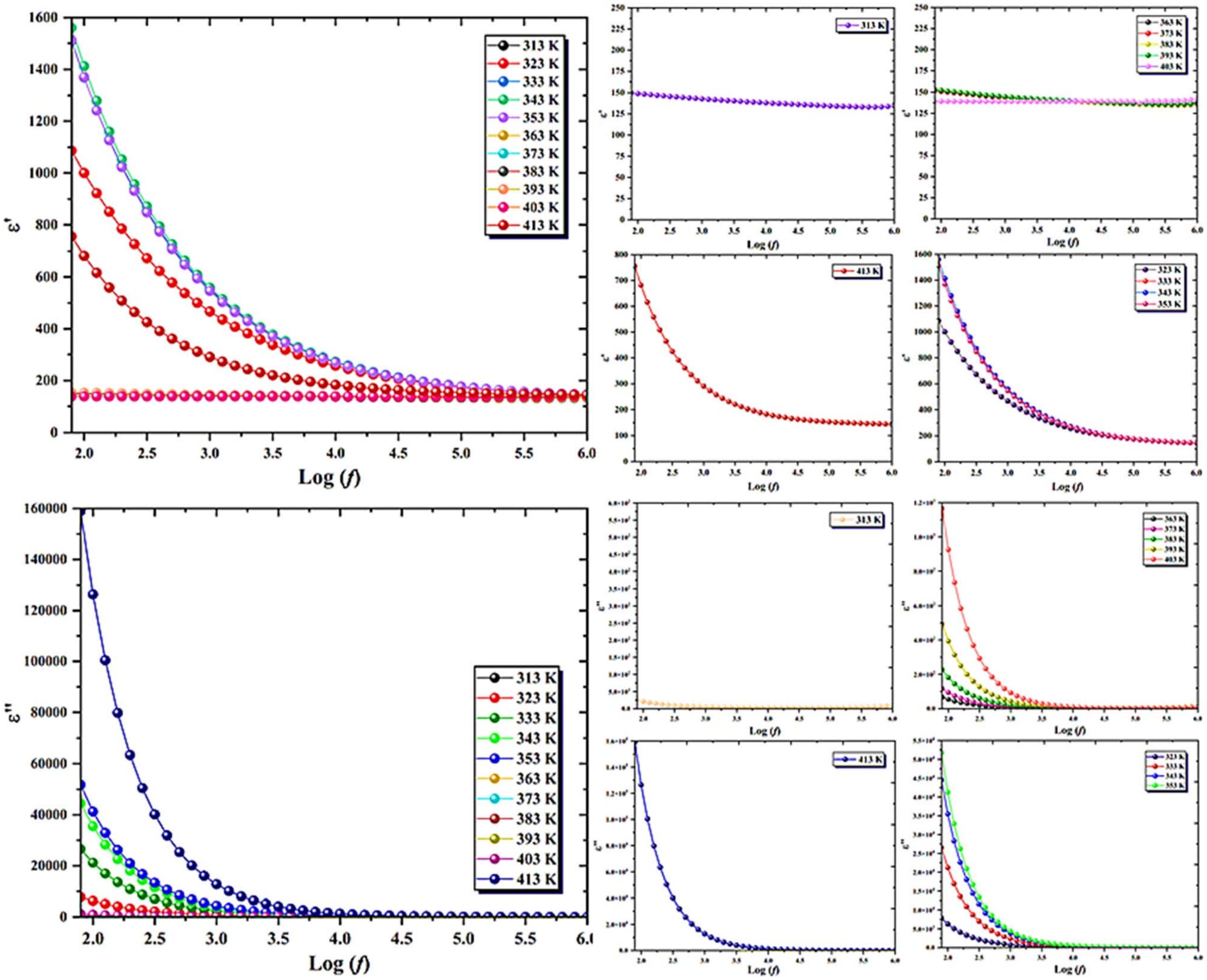

Fig. 16 Dielectric real and imaginary parts of permittivity (ε′ and ε″) as a function of frequency.

with pronounced peaks at intermediate frequencies and strong losses at lower frequencies, confirming that dielectric relaxation and conduction losses are tightly coupled.

The most revealing features emerge from the domain-resolved subfigures on the right, where the dielectric profiles are decomposed into four thermodynamically distinct temperature regimes. In the first domain (313 K), both ε′ and ε″ reach their maximum values, accompanied by strong dispersion and high dielectric losses, characteristic of sluggish dipolar orientation and intense space-charge accumulation at interfaces. The second domain (323–353 K) shows a sharp decline in ε′ and ε″, signifying partial relaxation of space charge and reduced interfacial polarization as thermal energy enhances carrier mobility. In the third domain (363–403 K), a moderate increase in permittivity appears, reflecting a phase with reactivated dielectric behavior but balanced polarization–relaxation dynamics. Finally, in the fourth domain (413 K), both ε′ and ε″ attain their lowest and flattest profiles, indicating a transition to bulk-dominated conduction where dipolar and interfacial polarization mechanisms become ineffective as carriers gain sufficient energy to overcome trapping barriers.

These well-defined dielectric fingerprints across the four regimes correspond closely with the conduction domains identified in Fig. 14, confirming that the electrical response is governed by temperature-induced structural transitions. Similar trends, initial high permittivity followed by thermal attenuation, have been reported in related hybrid perovskites and layered organometallics, where dynamic rearrangements of organic cations and inorganic sublattices modulate dielectric functionality.[44,45] The observed combination of extremely high low-frequency permittivity, tunable dielectric loss, and thermally responsive behavior positions $(C_8H_{14}N_2)[SbCl_5]$ as a promising candidate for tunable capacitors, electro-optic modulators, and phase-change dielectric devices.

4 Conclusion

In this study, the antimony-based organic–inorganic hybrid $(C_8H_{14}N_2)[SbCl_5]$ was comprehensively characterized through integrated thermal, optical, electrical, and theoretical analyses. The material exhibits a direct optical band gap of 2.77 eV, consistent with the DFT-derived HOMO–LUMO gap (2.7 eV).

Photoluminescence spectra display a strong green–yellow emission at 571 nm, with CIE coordinates confirming efficient radiative recombination and low structural disorder, supported by a sharp absorption edge and a small Urbach energy (177 meV).

Thermal studies (DSC) revealed three endothermic transitions at 323, 358, and 408 K, corresponding to structural reorganizations that directly influence dielectric behavior. These transitions correlate with the electrical response observed by impedance spectroscopy and conductivity measurements, which show four relaxation regimes characterized by frequency dispersion, non-Debye relaxation, and distinct activation energies, evidencing phase-dependent charge transport mechanisms.

Theoretical calculations (DFT and TD-DFT) provided a detailed picture of the compound's electronic structure and excited-state dynamics. DOS and orbital analyses confirmed significant inorganic-to-organic charge delocalization from the $[SbCl_5]^{2-}$ anion to the π-conjugated pyridyl ring. Topological analyses (MEP, RDG-NCI, ELF, LOL) revealed localized electron density regions, hydrogen bonds, and van der Waals interactions that stabilize the lattice and facilitate charge mobility.

Altogether, these findings establish $(C_8H_{14}N_2)[SbCl_5]$ as a structurally stable, optically active, and electrically tunable hybrid halometallate. Its combination of direct band gap, strong photoluminescence, multi-regime dielectric response, and efficient charge-transfer behavior underscores its potential for optoelectronic, dielectric, and thermoresponsive device applications. Future investigations will focus on its integration into functional devices and the evaluation of long-term operational stability.

Conflicts of interest

The authors declare that they have no known competing financial interests or personal relationships that could have appeared to influence the work reported in this paper.

Data availability

The raw/processed data required to reproduce these findings are available and can be sent if requested.

CCDC 2382366 contains the supplementary crystallographic data for this paper.[46]

Supplementary information is available. See DOI: https://doi.org/10.1039/d5ra06615h.

Acknowledgements

I would like to thank the Principal Engineer of the physics department of the Faculty of Sciences of Sfax Mrs DAMMAK Sameh for carrying out the chemical analyses by FTIR spectroscopy and UV-visible spectroscopy.

References

1 A. D. Nicholas, *et al.*, Low-Dimensional Hybrid Indium/Antimony Halide Perovskites: Supramolecular Assembly and Electronic Properties, *J. Phys. Chem. C*, 2020, **124**, 24485–24494.

2 A. Azmy, *et al.*, Synthesis and Optical Properties of One Year Air-Stable Chiral Sb(III) Halide Semiconductors, *Inorg. Chem.*, 2023, **62**, 20142–20152.

3 A. Piecha-Bisiorek, *et al.*, Correlation between Crystal Structures and Polar (Ferroelectric) Properties of Hybrids of Haloantimonates(III) and Halobismuthates(III), *Inorg. Chem. Front.*, 2020, **7**, 2107–2128.

4 R. Jakubas, *et al.*, Towards Ferroelectricity-Inducing Chains of Halogenoantimonates(III) and Halogenobismuthates(III), *RSC Adv.*, 2021, **11**, 1217–1225.

5 S. Qi, *et al.*, Organic–Inorganic Hybrid Antimony(III) Halides for Second Harmonic Generation, *Cryst. Growth Des.*, 2022, **22**, 6545–6553.

6 A. Koliogiorgos, *et al.*, Electronic and Gap Properties of Sb and Bi Based Halide Perovskites: An *Ab-Initio* Study, *arXiv*, 2017, preprint, arXiv:1711.04846, DOI: 10.48550/arXiv.1711.04846.

7 D.-Y. Hu, *et al.*, Revealing Structural, Elastic, Electronic and Optical Properties of Potential Perovskites K_2CuBiX_6 (X=Br, Cl) Based on First-Principles, *J. Solid State Chem.*, 2022, **310**, 123046.

8 J. Lin, *et al.*, Zero-Dimensional Lead-Free Halide with Indirect Optical Gap and Enhanced Photoluminescence by Sb Doping, *J. Phys. Chem. Lett.*, 2022, **13**, 198–207.

9 Y.-C. Peng, *et al.*, Selective Luminescence Response of a Zero-Dimensional Hybrid Antimony(III) Halide to Solvent Molecules: Size-Effect and Supramolecular Interactions, *Inorg. Chem.*, 2021, **60**, 17837–17845.

10 R. L. Ayscue, *et al.*, Structure–Property Relationships in Photoluminescent Bismuth Halide Organic Hybrid Materials, *Inorg. Chem.*, 2021, **60**, 9727–9744.

11 M. J. Panjikaran, *et al.*, Solution-Free Melt-Grown $CsGeI_3$ Polycrystals for Lead-Free Perovskite Photovoltaics: Synthesis, Characterization, and Theoretical Insights, *J. Electron. Mater.*, 2024, **53**, 6090–6097.

12 A. Ayyaz, *et al.*, Structural, Morphological, Elastic, Optoelectronic and Thermoelectric Properties of Lead-Free Double Perovskite $Na_2AgBiBr_6$ for Photovoltaic Applications: Experimental and DFT Insight, *Ceram. Int.*, 2024, **50**, 15261–15272.

13 W. Boujelbene, *et al.*, Synthesis,structural and optical properties of a new orthochromite compound prepared by sol-gel method, *J. Mater. Sci.: Mater. Electron.*, 2025, **36**, 936.

14 K. Guithi, *et al.*, Electrical and optical properties of environmental friendly $Li_{(1-x)}Sm\ x/_3NbO_3$ ceramics for high-temperature energy storage applications, *J. Opt.*, 2023, **52**, 1494–1506.

15 K. Kahouli, *et al.*, Optical properties analysis of the new $(C_9H_{14}N)_3BiCl_6$ compound by UV-Visible measurements, *Indian J. Phys.*, 2022, 2797–2805.

16 Y.-N. Wang, *et al.*, Band Gap Modulation of Organic–Inorganic Sb(III) Halide by Molecular Design, *CrystEngComm*, 2022, **24**, 1007–1013.

17 Y. Zhou, *et al.*, Enhanced Photoluminescence in Sb(III)-Based Hybrid Halides *via* Organic Cation Engineering, *Adv. Opt. Mater.*, 2023, **11**, 2202456.

18 X. Liu, *et al.*, Dielectric Relaxation Behavior in Zero-Dimensional Sb(III) Hybrid Halides, *J. Mater. Chem. C*, 2022, **10**, 1234–1242.

19 H. Chen, *et al.*, Ferroelectric Properties of Sb(III)-Based Organic–Inorganic Hybrids, *Appl. Phys. Lett.*, 2021, **119**, 052901.

20 Y. Gao, *et al.*, Optoelectronic Performance of Sb(III) Halide Hybrids in Light-Emitting Diodes, *ACS Appl. Mater. Interfaces*, 2022, **14**, 5678–5685.

21 L. Zhang, *et al.*, Thermal Stability and Dielectric Properties of Sb(III) Hybrid Halides, *J. Phys. Chem. C*, 2023, **127**, 3456–3463.

22 J. Wang, *et al.*, Photophysical Properties of Sb(III)-Based Halide Hybrids for Optoelectronic Applications, *Chem. Mater.*, 2022, **34**, 7890–7898.

23 M. Li, *et al.*, Charge Transport in Sb(III) Hybrid Halide Semiconductors, *Adv. Funct. Mater.*, 2023, **33**, 2301234.

24 Y. Xu, *et al.*, Environmental Stability of Lead-Free Sb(III) Halide Hybrids, *ACS Sustain. Chem. Eng.*, 2022, **10**, 11234–11242.

25 Q. Zhao, *et al.*, Sb(III) Halide Hybrids: A Sustainable Approach to Optoelectronics, *Green Chem.*, 2023, **25**, 567–575.

26 S. Kim, *et al.*, Composite Materials Incorporating Sb(III) Halide Hybrids for Enhanced Optoelectronic Applications, *Adv. Mater.*, 2024, **36**, 2304567.

27 H. Lee, *et al.*, Flexible Electronics Based on Sb(III) Hybrid Halide Materials, *Nano Energy*, 2023, **105**, 107890.

28 M. A. Garcia, *et al.*, Integration of Sb(III) Halide Hybrids into Photonic Devices: Challenges and Opportunities, *ACS Photonics*, 2024, **11**, 1234–1245.

29 A. Alibi, N. Elleuch, S. Shova and M. Boujelbene, A new hybrid Sb-based compound, *J. Mol. Struct.*, 2025, **1324**, 140857.

30 T. Lu and F. Chen, Multiwfn: A multifunctional wavefunction analyzer, *J. Mol. Struct.*, 2012, **1006**, 84–92.

31 N. Zhanpeisov, M. Matsuoka, H. Yamashita and M. Anpo, NO molecule interaction study, *J. Phys. Chem. B*, 1998, **102**, 6915.

32 N. Nicklass, M. Dolg, H. Stoll and H. Preuss, Pseudopotential study of noble gases, *J. Chem. Phys.*, 1995, **102**, 8942.

33 M. J. Frisch, G. W. Trucks, H. B. Schlegel, G. E. Scuseria and M. A. Robb, *et al.*, *Gaussian 09, Revision E.01*, Gaussian, Inc., Wallingford CT, 2013.

34 R. Dennington, T. A. Keith and J. M. Millam, *GaussView, Version 5*, Semichem Inc., Shawnee Mission, KS, 2009.

35 E. Caponetti, L. Pedone, D. Chillura Martino, V. Panto and V. Turco Liveri, Dye-doped surfactant aggregates, *Mater. Sci. Eng., C*, 2003, **23**, 531.

36 N. Tounsi, A. Barhoumi, F. C. Akkari, M. Kanzari, H. Guermazi and S. Guermazi, Optical and structural study of PbS thin films, *Vacuum*, 2015, **121**, 9.

37 S. R. Chalana, V. Ganesan and V. P. Mahadevan Pillai, Study on ZnO:Eu thin films, *AIP Adv.*, 2015, **5**, 107207.

38 N. M. O'Boyle, A. L. Tenderholt and K. M. Langner, CCLib: a library for computational chemistry, *J. Comput. Chem.*, 2008, **29**, 839.

39 R. K. Singh, S. K. Verma and P. D. Sharma, DFT-based interaction analysis, *Int. J. ChemTech Res.*, 2011, **3**, 1571.

40 C. G. Zhan, J. A. Nichols and D. A. Dixon, Molecular properties *via* orbital energies, *J. Phys. Chem. A*, 2003, **107**, 4184.

41 S. Kumar, V. K. Shukla and R. N. P. Choudhary, Study of dielectric and ferroelectric properties, *Asian J. Res. Chem.*, 2015, **8**, 4.

42 S. Zhang, J. Huang, X. Guo, Y. Zhao, J. Liang, C. Ma, H. Gao and F. Wu, Bismuth-based hybrid solar absorbers, *J. Am. Chem. Soc.*, 2021, **143**, 15821.

43 H. Ali, A. J. Kadhim, K. N. Hussein and A. T. Nahr, Study of electronic properties of perovskites, *J. Mater. Sci.: Mater. Electron.*, 2022, **33**, 374.

44 A. K. Jonscher, *Dielectric Relaxation in Solids*, Chelsea Dielectrics Press, London, 1983.

45 G. Giorgi and K. Yamashita, Lead-free perovskite exploration, *J. Mater. Chem. A*, 2015, **3**, 8981.

46 CCDC 2382366: Experimental Crystal Structure Determination, 2025, DOI: **10.5517/ccdc.csd.cc2kz1j4**.